Light-tunable 1T-TaS2 charge-density-wave oscillators

Zhu, Chao; Chen, Yu; Liu, Fucai; Zheng, Shoujun; Li, Xiaobao; Chaturvedi, Apoorva; Zhou, Jiadong; Fu, Qundong; He, Yongmin; Zeng, Qingsheng; Fan, Hong Jin; Zhang, Hua; Liu, Wen-Jun; Yu, Ting; Liu, Zheng

Light-Tunable 1T-TaS₂ Charge-Density-Wave Oscillators

Chao Zhu[1,#], Yu Chen[2,#], Fucai Liu[1,3,], Shoujun Zheng[2,4], Xiaobao Li[5], Apoorva Chaturvedi[1],*

Jiadong Zhou[1], Qundong Fu[1], Yongmin He[1], Qingsheng Zeng[1], Hong Jin Fan[2,4], Hua Zhang[1],

Wen-Jun Liu[6], Ting Yu[2,], Zheng Liu[1,7,8,*]*

[1]Center for Programmable Materials, School of Materials Science and Engineering, Nanyang

Technological University, Singapore 639798, Singapore.

[2]Division of Physics and Applied Physics, School of Physical and Mathematical Sciences,

Nanyang Technological University, Singapore 637371, Singapore.

[3]School of Optoelectronic Science and Engineering, University of Electronic Science and

Technology of China, Chengdu, 610054, China.

[4]Centre for Disruptive Photonic Technologies, School of Physics and Mathematics Sciences,

Nanyang Technological University, Singapore 637371, Singapore.

[5]School of Civil Engineering, Hefei University of Technology, Hefei 230009, China.

[6]State Key Laboratory of ASIC and System, School of Microelectronics, Fudan University,

Shanghai 200433, China.

[7]NOVITAS, Nanoelectronics Centre of Excellence, School of Electrical and Electronic

Engineering, Nanyang Technological University, Singapore 639798, Singapore.

[8]CINTRA CNRS/NTU/THALES, UMI 3288, Research Techno Plaza, Singapore 637553, Singapore.

*Email: fucailiu@gmail.com (F.L.), yuting@ntu.edu.sg (T.Y.), z.liu@ntu.edu.sg (Z.L.)

# C.Z. and Y.C. contributed equally to the work.

Abstract: External stimuli-controlled phase transitions are essential for fundamental physics and design of functional devices. Charge density wave (CDW) is a metastable collective electronic phase featured by the periodic lattice distortion. Much attention has been attracted to study the external control of CDW phases. Although much work has been done in the electric-field-induced CDW transition, the study of the role of Joule heating in the phase transition is insufficient. Here, using the Raman spectroscopy, the electric-field-driven phase transition is *in situ* observed in the ultrathin $1T\text{-}TaS_2$. By quantitative evaluation of the Joule heating effect in the electric-field-induced CDW transition, it is shown that Joule heating plays a secondary role in the nearly commensurate (NC) to incommensurate (IC) CDW transition while it dominants the IC-NC CDW transition, providing a better understanding of the electric field-induced phase transition. More importantly, at room temperature, light illumination can modulate the CDW phase and thus tune the frequency of the ultrathin $1T\text{-}TaS_2$ oscillators. This light tunability of the CDW phase transition is promising for multifunctional device applications.

Keywords: $1T\text{-}TaS_2$, phase transition, *in situ* Raman Spectroscopy, light tunability, oscillator

In low-dimensional metals such as layered cuprates[1-3] and transition metal dichalcogenides (TMDs),[4-11] periodic lattice distortion is often observed at low temperatures, which is induced by

various factors such as the strong electron-phonon interaction[12] and electron-electron interaction.[13] This lattice distortion results in the spatial modulation of charge carrier densities, giving rise to the metastable phase of charge density wave (CDW). Recently, the layered $1T\text{-}TaS_2$ has drawn intensive attentions due to its enriched CDW phases.[11,14-28] For instance, there are mainly three CDW phases in $1T\text{-}TaS_2$: the incommensurate CDW (ICCDW) phase from 550 K to 350 K, the nearly commensurate CDW (NCCDW) phase from 350 K to 180 K and the commensurate CDW phase below 180 K, which is stabilized by the Mott insulator state.[11] With such a rich set of charge ordered states, $1T\text{-}TaS_2$ provides a good platform for the controllable manipulation of various phases. The transitions between these CDW phases can be influenced by a variety of factors including the thickness,[18,19] the gate bias,[18] the in-plane electric field,[19-23] cooling rate,[21] the substrate[26] and the ultrashort light or current excitation.[14,27] For example, the NCCDW-CCDW phase transition disappears when $1T\text{-}TaS_2$ is thinner than 10 nm.[18] Although there are many studies on the electric-field-driven CDW phase transition of the layered $1T\text{-}TaS_2$,[19-23] limited research has been done to provide direct evidence of the phase transition or clearly demonstrate the underlying reason of the phase transition. By utilizing the electric-field-driven CDW phase transition, functional electronic devices could be designed.[23-25] For instance, a voltage-controlled oscillator (VCO) based on $1T\text{-}TaS_2\text{-}BN\text{-}graphene$ was fabricated and the modulation of the oscillation by gate voltage was demonstrated.[23] Moreover, by integrating the two-dimensional CDW based oscillators, a neural network for pattern recognition was constructed.[25] Achieving various ways to manipulate such electronic devices is fundamentally interesting and technologically important, for integrated electronic and optoelectronic device applications.

In this work, we systematically studied the CDW phase transition of $1T\text{-}TaS_2$ under electric field as well as light illumination. The electric-field-induced CDW phase transition process was

investigated using the *in situ* Raman spectroscopy, providing a clear evidence of the transition between NCCDW and ICCDW phase. The significance of Joule heating (JH) effect in this phase transition was investigated by analyzing the temperature-dependent *I-V* characteristics. Furthermore, we introduced a way to manipulate the oscillation of ultrathin 1T-TaS$_2$ based CDW oscillators by light illumination. We found that the frequency of the oscillator constructed by 1T-TaS$_2$ could be well controlled by the illuminated power of the laser. For the demonstrated device, the frequency could be tuned up to around 30%. Light controllability of the CDW oscillator will provide more options for the applications of CDW materials in mid- to high-frequency electronic devices.

RESULTS AND DISCUSSION

Characterization of 1T-TaS$_2$. Figure 1a shows the crystal structure of 1T-TaS$_2$ with an interlayer distance of 5.85 Å. According to Peierls' theory,[12,29] at low temperature, the Peierls instability will induce lattice distortions where twelve nearby Ta atoms move towards the central Ta atom to form an atom cluster called David star (Figure 1b). In the ICCDW phase, the lattice is slightly distorted and there is no David star domain. When the crystal temperature is below 350 K, the crystal turns into the NCCDW phase, which is partially filled by David star domains. While below 180 K, the crystal is fully filled by David stars which form the CCDW superlattice. It has been reported that the CCDW phase may be absent in thin samples.[18,19] In order to study the phase transitions in 1T-TaS$_2$, the chemical vapour transport method was used to prepare 1T-TaS$_2$ single crystals. Then thin 1T-TaS$_2$ flakes were mechanically exfoliated onto the Si wafer with a 285-nm-thick SiO$_2$ layer. A typical optical image of thin 1T-TaS$_2$ films is shown in Figure 1c, accompanied by the AFM image Figure 1d. Figure 1e displays the height profile of the line marked in Figure 1c, showing that the maximum thickness is about 10 nm.

Raman spectroscopy is a sensitive tool for the identification of lattice distortion and phase transition. We first conducted the temperature-dependent Raman spectra to confirm the CDW phase transition in 1T-TaS$_2$. The Raman signals of a 9.4-nm-thick 1T-TaS$_2$ sample were collected under the 532-nm laser excitation with a 90-s integration time at 80 K, which are shown in Figure 1f. The CDW lattice distortion induces the appearance of peaks between 50-100 cm^{-1} and at around 240 cm^{-1}, which is consistent with previous reports.[15-17] As the temperature increases from 80 K, the intensity of these peaks decreases, indicating that the CDW lattice distortion is partially relaxed. Above 350 K, the sample goes through the NC-IC CDW phase transition, featured by the disappearance of the CDW-induced Raman peaks. The change of temperature-dependent Raman spectra is consistent well with the CDW phase transition. It provides us a way for *in situ* monitoring the CDW phase transition.

***In situ* Raman spectroscopy for the electric-field-induced CDW phase transition.** It is known that 1T-TaS$_2$ can go through a transition from a high resistance state to a low resistance state as the in-plane electrical bias increases.[19-21,23] This is explained by the phase transition between different CDW phases. However, evidences of the phase transition by *in situ* characterizations are insufficient. Here we report the evidence of this phase transition by the *in situ* Raman spectra measurement. Since at high temperatures the intensity of Raman signals of 1T-TaS$_2$ are weakened, we performed the *in situ* Raman test at relatively low temperatures. As shown in Figure 2a, at 80 K, the two-probe *I-V* sweeping test was first performed to determine the upper and lower threshold voltage (V_H and V_L, shown by black dots), which were 2.43 V and 2.22 V, respectively. Then *in situ* Raman spectra were collected while the in-plane voltage was applied to the sample. For simplification, the voltage was set to several key values in sequence (0 V, 2.00 V, 2.25 V, 2.50 V, 2.25 V and 2.00 V). The current measured during the *in situ* Raman test was

consistent with the previous *I-V* characteristics in the first step, ensuring the reliability of the *in situ* Raman test. As shown in Figure 2b, at 0 V, 1T-TaS$_2$ shows an NCCDW phase according to the temperature-dependent Raman spectra. As the voltage increases from 0 V to 2.25 V, the A$_{1g}$ (70 and 76 cm^{-1}) and E$_g$ (60 and 93 cm^{-1}) peaks still remain, indicating that the CDW phase is unchanged. When the voltage increases to 2.50 V, which is higher than V_H (2.43 V), A$_{1g}$ and E$_g$ peaks disappear, indicating that the sample undergoes a phase transition from NCCDW to ICCDW phase. When the voltage sweeps back to 2.25 V, since it is still above V_L (2.22 V), the sample stays at ICCDW phase, as verified by the Raman spectra. When the voltage sweeps back to 2.00 V, which is below V_L, the sample changes back to the NCCDW phase, featured by the reappearance of the CDW Raman peaks. The change of intensity of the A$_{1g}$ peak at 76 cm^{-1} (pointed out by the arrow in Figure 2b) is depicted by the red dash line in Figure 2a, confirming the non-destructive *in situ* probe of the electric-field-induced phase transition. *In situ* Raman test was also performed at 220 K, showing the same behaviour (see Supporting Information).

Role of Joule heating effect. The current-induced Joule heating effect will inevitably change the local temperature of the sample, which may influence the CDW phase transitions. Although it has been pointed out that the phase transition induced by electric field is attributed to both the field-induced depinning and the Joule heating effect,[12,21,22] the role of Joule heating effect is still not clearly demonstrated. Thus, we further performed a more quantitative evaluation of the Joule heating effect. A further two-probe *I-V* test was carried out to characterize the CDW phase transition driven by the in-plane electric field at different temperatures (Figure 3a). As the temperature increases from 200 K to 330 K, the threshold voltage V_H decreases from 0.89 V to 0.40 V and V_L decreases from 0.82 V to 0.40 V. To examine the effect of Joule heating in the phase transition, the Joule heating (JH) rate (per unit length) at the NC-IC and IC-NC phase transition

6

points (V_H and V_L) was calculated and the Joule-heating-induced temperature increase of the sample was evaluated.

In order to better understand our situation, considering the Joule heat generation and dissipation on the silicon wafer,[30,31] we choose the heat equation along the TaS$_2$ device as:

$$A\frac{\partial}{\partial x}\left(k\frac{\partial T_{JH}}{\partial x}\right) + P - g(T_{JH} - T) = 0 \tag{1}$$

where A is the cross-section of the TaS$_2$ device, k is the thermal conductivity of TaS$_2$,[32] P is the heat generation rate per unit length and g is the thermal conductance to the substrate or electrode per unit length.[30,31,33-38] T_{JH} is the sample temperature under Joule heating and T is the temperature of the substrate or electrode. For simplification, within the TaS$_2$ channel, we consider a uniform Joule heating case where $P = I^2 R_{ch}/L_{ch}$ (I is the current, R_{ch} is the channel resistance and L_{ch} is the channel length). The contact resistance is estimated to be 8 % of the total resistance according to our previous work.[19] While in the electrode contact area, considering the current crowding effect,[31,39] the potential distribution is described by:

$$V(x) = \frac{I}{W}\sqrt{\rho_c R_{sh}}\frac{cosh(x/L_T)}{sin\ (L_c/L_T)} \tag{2}$$

where W is the channel width, ρ_c is the contact resistivity, R_{sh} is the TaS$_2$ sheet resistance, L_c is the contact length, L_T is the contact transfer length and x is the distance from the outer edge of electrode (see details in Supporting Information). The heating generation rate is then defined by $P = IdV(x)/dx$. The heat equation was solved by combining the heat dissipation in the channel and contact region using the finite element method. As shown in Figure 3b, the Joule heating (JH) rate ($P = I^2 R_{ch}/L_{ch}$) at V_H and V_L decreases linearly with respect to the temperature, which is consistent with the fact that V_H and V_L are proportional to $(1-T/T_{NC-IC})^{1/2}$, where T_{NC-IC} is the NC-IC phase transition temperature.[23] $T_{JH} - T$ also decreases linearly with increasing temperature.

According to Figure 3b, first, for the NC-IC phase transition at V_H, Joule heating accounts partially for the transition by heating the sample to some level below the transition temperature $T_{NC\text{-}IC}$.[18] As T increases from 200 K to 330 K, T_{JH} increases from 290 K to 355 K. The temperature-dependent T_{JH} is consistent with the temperature-dependent sample resistance at V_H.[19] The field-induced depinning effect makes a major contribution on the abrupt NC-IC transition. Second, the IC-NC phase transition at V_L is mainly determined by the Joule-heating-induced temperature change. As T increases from 200 K to 320 K, T_{JH} increases from 350 K to 365 K, which is a little bit higher than the IC-NC transition temperature $T_{IC\text{-}NC}$[18] and does not show strong dependence on temperature. As the voltage decreases below V_L, Joule heat generation decreases so that T_{JH} drops below $T_{IC\text{-}NC}$, leading to the IC-NC phase transition. This is consistent with previous report that the sample resistance is almost the same just before the IC-NC transition regardless of the environment temperature.[19] Moreover, if we take $T_{JH} - T = 0$ as the point where phase transition happens without Joule heating, we get $T_{NC-IC} = 382$ K and $T_{IC-N} = 368$ K, which is consistent with the fact that $T_{NC-IC} > T_{IC-NC}$.[18] Note that T_{NC-IC} and T_{IC-} are a little bit higher than the reported values, which might be attributed to the neglect of temperature dependence of thermal conductivity[32] and the estimation of contact resistance and electrode thermal conductivity when we solve the heat equation.

Light-tunable 1T-TaS$_2$ CDW oscillator. Inspired by the role of Joule heating in the phase transition, laser thermal effect provides us an alternative way to control the phase transition in 1T-TaS$_2$. A beam of 635 nm laser was shined onto the device with the electrical bias applied. As shown is Figure 4a, with the laser intensity increasing, the hysteresis *I-V* curve shifts to the left. *I-V* curves in the dark repeated well before and after 160 mW/cm^2 shining, indicating that no obvious degradation occurred. To understand the mechanism of light tuning phase transition, the time

evolution of the current with the laser on/off was investigated. The current was measured with a fixed in-plane bias (0.51 V) applied on the sample while the laser was turned on/off to test the response of the sample. As shown in Figure 4b, the laser is turned on at 10 s and keeps shining until it was turned off at 130 s. When the laser is on, the current increases slowly. In the case of 40, 80 and 120 mW/cm^2, there is no abrupt change in current, indicating that no phase transition occurs. However, when the intensity is 160 mW/cm^2, the current reaches the critical value at about 90 s and then the sample undergoes the NC-IC phase transition, leading to a sharp rise in current from 0.41 mA to 0.70 mA. When the laser is turned off, the current decreases. The sample goes through several minor steps before it finally returns to the NC phase, which is accompanied by a sudden drop in the current at 250 s. The current evolution during the increasing or decreasing process can be well fitted exponentially (see Supporting Information). The time constants of current rising and decaying for different laser intensities are shown in Figure 4c. Since the evolution of the current is very slow, we attribute this light tuning of the phase transition to the thermal effect. The change of Joule heating rate with the intensity is shown in Figure 4d. The decrease in Joule heating rate at V_H for 160 mW/cm^2 is about 0.019 mW/μm, with respect to that for 0 mW/cm^2. By comparing with Figure 3b, it shows that this laser-heating-induced change corresponds to about 6 K change in environment temperature.

To take the advantage of the light-tunable phase transition, we configured an oscillator by integrating the 1T-TaS$_2$ device with a 1000 Ω resistor. The configuration is illustrated in Figure 5a. A resistor is connected to 1T-TaS$_2$ with the input voltage applied by a source meter on the other side. The output signal is the voltage across the 1T-TaS$_2$ and is monitored by an oscilloscope. Figure 5b illustrates the mechanism of the oscillator. By matching the resistor with the 1T-TaS$_2$ and tuning the value of input voltage, the voltage loaded on the 1T-TaS$_2$ can be set to a value a

little bit larger than the upper threshold. In this way, the 1T-TaS$_2$ will go through the NC-IC CDW phase transition, accompanied by the sharp decrease in resistance. In turn, the voltage loaded on the 1T-TaS$_2$ will decrease, leading to its phase transition back to the NCCDW phase. Then the voltage loaded on 1T-TaS$_2$ will increase subsequently. In this way, the 1T-TaS$_2$ will oscillate between NCCDW and ICCDW phases and the output voltage will oscillate at the same time. By changing the V_{DC}, we found that the frequency of the output signal (V_{OUT}) could be tuned and there was a monotonically decreasing region between 3.82 and 4.05 V (Figure 5c). The frequency of V_{OUT} is determined by the charging and discharging time of the capacitor within the circuit, which is then related to factors including sample resistance and threshold voltage (V_H and V_L).[23] Furthermore, V_H and V_L can be tuned by the laser intensity (see Figure 4a), providing the possibility to tune the oscillator frequency by the light. Based on this, we set the input voltage to a fixed value and shined the light onto the device. By changing the intensity of the light, the frequency of the output voltage could be tuned up to about 30%, as shown in Figure 5d and 5e. Meanwhile, the waveforms of the oscillation under different light intensities show a high-quality periodicity. The values of oscillation frequency can be calculated from the *I-V* characteristics,[23] which are plotted with dash lines in Figure 5e, fitting well to the experimental values. It needs to be mentioned that the oscillation waveforms in Figure 5d are kind of asymmetric, which is much more obvious at higher intensities. We attribute it to the asymmetric status of TaS$_2$ set by load voltage V_{DC}. For V_{DC} = 3.90 V, the intersections of the load line and the hysteresis *I-V* curve are not exactly located at the middle of the loop but shift towards the top of the loop as light intensity increases (see the Figure S4a). As a result, TaS$_2$ stays a longer time at the low resistive ICCDW phase, which leads to a longer time for the transition from the ICCDW phase to the NCCDW phase. The light tunability of the oscillation frequency and waveform adds more possibilities for its applications in

compact on-chip oscillators, such as pattern recognition[25,40] and fast neural spiking generation.[41,42] On the other hand, the local heating nature of the laser also inspires the integration of other local heating techniques[30,43] into the CDW material based oscillators.

CONCLUSION

In summary, we report the non-destructive *in situ* Raman spectra evidence of the in-plane electric-field-induced phase transition between NCCDW and ICCDW. The quantitative evaluation of Joule heating effect shows that Joule heating only plays a secondary role in the NC-IC CDW transition while the IC-NC CDW transition is mainly determined by Joule-heating-induced temperature change of the sample. Moreover, the light tunability of the phase transition is demonstrated and the light could be used to tune the frequency and waveform of the $1T$-TaS_2 based oscillators. The results demonstrated here will be of much help for understanding the physics behind the electric-field-induced CDW phase transition, as well as device applications of CDW materials.

METHODS

Synthesis of 1T-TaS₂. For the single crystal growth of $1T$-TaS_2, the stoichiometric amount of tantalum powder (99.97%) and sulfur pieces (99.9995%) were used. The materials (Ta and S) and a small amount (2 mg/cc) of iodine spheres were sealed in an evacuated quartz tube (ampoule) with an inner pressure in the range of 10^{-5} Torr to 10^{-6} Torr, which were then subjected to a two-zone temperature profile of 950 to 900 °C for a period of 168 hours. After this, the temperatures were lowered down, and the plate-like crystals were obtained.

Device fabrication. Thin $1T$-TaS_2 films were exfoliated onto the SiO_2/Si substrate from bulk crystals using the Scotch tape. The electrode patterns were then defined by the electron beam lithography. Metal electrodes (5 nm Cr / 50 nm Au) were deposited by thermal evaporator.

In situ Raman test. The *in situ* Raman spectra were measured by a WITec Raman system with the sample loaded on a Linkam temperature control stage in vacuum. A beam of 532-nm excitation laser was shined onto the sample through a $50 \times$ long working distance objective, with a power of 1 mW. Meanwhile, the in-plane electric field was applied by a semiconductor analyser (Keithley 4200).

Temperature-dependent I-V characterization and simulation of Joule heating. The temperature-dependent *I-V* curves were measured by Keithley 2450 Sourcemeter while the devices were loaded on a Linkam temperature control stage in vacuum. The simulation of Joule heating was performed by finite element method using a simplified 1D model (see the Supporting Information).

Light-tuned 1T-TaS$_2$ oscillator measurement. Samples were loaded in a MicroXact probe station with pressure below 10^{-5} Torr while the DC voltage was applied by Keithley 2450 Sourcemeter. The light was illuminated by a 635-nm laser diode. And the output voltage was measured by a mixed domain oscilloscope (Tektronix MDO3052).

ASSOCIATED CONTENT

Supporting Information.

The Supporting Information is available free of charge on the ACS Publications website.

In situ Raman spectra of electric field induced phase transition in $1T$-TaS_2. Evaluation of Joule heating effect in the phase transition. Fitting of the current evolution under laser illumination. Additional details of $1T$-TaS_2 based oscillator.

AUTHOR INFORMATION

Corresponding Author

*Email: fucailiu@gmail.com (F.L.), yuting@ntu.edu.sg (T.Y.), z.liu@ntu.edu.sg (Z.L.)

Author Contributions

C.Z., F.L. and Z.L. conceived and designed the research. C.Z. fabricated devices and oscillator measurement. Y.C. performed the Raman measurement and data analysis. C.Z. and S.Z. performed the temperature-dependent *I-V* measurement. C.Z. and X.L. performed the simulation and calculation. A.C. synthesized single crystals. J.Z., Q.F., Y.H., Q.Z., H.F., H.Z., W.L. and T.Y. contributed to data analysis and discussions. T.Y. and Z.L. supervised the research. Z.C., F.L. and Z.L. prepared the manuscript with comments from all authors. # C.Z. and Y.C. contributed equally.

Notes

The authors declare no competing financial interest.

REFERENCES

(1) Achkar, A. J.; He, F.; Sutarto, R.; McMahon, C.; Zwiebler, M.; Hucker, M.; Gu, G. D.; Liang, R.; Bonn, D. A.; Hardy, W. N.; Geck, J.; Hawthorn, D. G. Orbital Symmetry of Charge-Density-Wave Order in $La_{1.875}Ba_{0.125}CuO_4$ and $YBa_2Cu_3O_{6.67}$. *Nat. Mater.* **2016**, *15*, 616-620.

(2) Chang, J.; Blackburn, E.; Ivashko, O.; Holmes, A. T.; Christensen, N. B.; Hucker, M.; Liang, R.; Bonn, D. A.; Hardy, W. N.; Rutt, U.; Zimmermann, M. V.; Forgan, E. M.; Hayden, S. M. Magnetic Field Controlled Charge Density Wave Coupling in Underdoped $YBa_2Cu_3O_{6+X}$. *Nat. Commun.* **2016**, *7*, 11494.

(3) Frano, A.; Blanco-Canosa, S.; Schierle, E.; Lu, Y.; Wu, M.; Bluschke, M.; Minola, M.; Christiani, G.; Habermeier, H. U.; Logvenov, G.; Wang, Y.; van Aken, P. A.; Benckiser, E.; Weschke, E.; Le Tacon, M.; Keimer, B. Long-Range Charge-Density-Wave Proximity Effect at Cuprate/Manganate Interfaces. *Nat. Mater.* **2016**, *15*, 831-834.

(4) Adelman, T. L.; Zaitsev-Zotov, S. V.; Thorne, R. E. Field-Effect Modulation of Charge-Density-Wave Transport in $NbSe_3$ and TaS_3. *Phys. Rev. Lett.* **1995**, *74*, 5264-5267.

(5) Miller, J. H., Jr.; Wijesinghe, A. I.; Tang, Z.; Guloy, A. M. Correlated Quantum Transport of Density Wave Electrons. *Phys. Rev. Lett.* **2012**, *108*, 036404.

(6) Samnakay, R.; Wickramaratne, D.; Pope, T. R.; Lake, R. K.; Salguero, T. T.; Balandin, A. A. Zone-Folded Phonons and the Commensurate-Incommensurate Charge-Density-Wave Transition in $1T-TaSe_2$ Thin Films. *Nano Lett.* **2015**, *15*, 2965-2973.

(7) Li, L. J.; O'Farrell, E. C.; Loh, K. P.; Eda, G.; Ozyilmaz, B.; Castro Neto, A. H. Controlling Many-Body States by the Electric-Field Effect in a Two-Dimensional Material. *Nature* **2016**, *529*, 185-189.

(8) Wilson, J. A.; Di Salvo, F. J.; Mahajan, S. Charge-Density Waves in Metallic, Layered, Transition-Metal Dichalcogenides. *Phys. Rev. Lett.* **1974**, *32*, 882-885.

(9) Di Salvo, F. J.; Moncton, D. E.; Waszczak, J. V. Electronic Properties and Superlattice Formation in the Semimetal $TiSe_2$. *Phys. Rev. B* **1976**, *14*, 4321-4328.

(10) Moncton, D. E.; Axe, J. D.; DiSalvo, F. J. Neutron Scattering Study of the Charge-Density Wave Transitions in 2H−$TaSe_2$ and 2H−$NbSe_2$. *Phys. Rev. B* **1977**, *16*, 801-819.

(11) Sipos, B.; Kusmartseva, A. F.; Akrap, A.; Berger, H.; Forro, L.; Tutis, E. From Mott State to Superconductivity in 1T-TaS_2. *Nat. Mater.* **2008**, *7*, 960-965.

(12) Grüner, G. The Dynamics of Charge-Density Waves. *Rev. Mod. Phys.* **1988**, *60*, 1129-1181.

(13) Halperin, B. I.; Rice, T. M. Possible Anomalies at a Semimetal-Semiconductor Transistion. *Rev. Mod. Phys.* **1968**, *40*, 755-766.

(14) Vaskivskyi, I.; Gospodaric, J.; Brazovskii, S.; Svetin, D.; Sutar, P.; Goreshnik, E.; Mihailovic, I. A.; Mertelj, T.; Mihailovic, D. Controlling the Metal-to-Insulator Relaxation of the Metastable Hidden Quantum State in 1T-TaS_2. *Sci. Adv.* **2015**, *1*, e1500168.

(15) Albertini, O. R.; Zhao, R.; McCann, R. L.; Feng, S.; Terrones, M.; Freericks, J. K.; Robinson, J. A.; Liu, A. Y. Zone-Center Phonons of Bulk, Few-Layer, and Monolayer 1T−TaS_2: Detection of Commensurate Charge Density Wave Phase through Raman Scattering. *Phys. Rev. B* **2016**, *93*, 214109.

(16) Fu, W.; Chen, Y.; Lin, J.; Wang, X.; Zeng, Q.; Zhou, J.; Zheng, L.; Wang, H.; He, Y.; He, H.; Fu, Q.; Suenaga, K.; Yu, T.; Liu, Z. Controlled Synthesis of Atomically Thin 1T-TaS_2 for Tunable Charge Density Wave Phase Transitions. *Chem. Mater.* **2016**, *28*, 7613-7618.

(17) He, R.; Okamoto, J.; Ye, Z.; Ye, G.; Anderson, H.; Dai, X.; Wu, X.; Hu, J.; Liu, Y.; Lu, W.; Sun, Y.; Pasupathy, A. N.; Tsen, A. W. Distinct Surface and Bulk Charge Density Waves in Ultrathin 1T−TaS_2. *Phys. Rev. B* **2016**, *94*, 201108.

(18) Yu, Y.; Yang, F.; Lu, X. F.; Yan, Y. J.; Cho, Y. H.; Ma, L.; Niu, X.; Kim, S.; Son, Y. W.; Feng, D.; Li, S.; Cheong, S. W.; Chen, X. H.; Zhang, Y. Gate-Tunable Phase Transitions in Thin Flakes of 1T-TaS$_2$. *Nat. Nanotechnol.* **2015**, *10*, 270-276.

(19) Zheng, S.; Liu, F.; Zhu, C.; Liu, Z.; Fan, H. J. Room-Temperature Electrically Driven Phase Transition of Two-Dimensional 1T-TaS$_2$ Layers. *Nanoscale* **2017**, *9*, 2436-2441.

(20) Tsen, A. W.; Hovden, R.; Wang, D.; Kim, Y. D.; Okamoto, J.; Spoth, K. A.; Liu, Y.; Lu, W.; Sun, Y.; Hone, J. C.; Kourkoutis, L. F.; Kim, P.; Pasupathy, A. N. Structure and Control of Charge Density Waves in Two-Dimensional 1T-TaS$_2$. *Proc. Natl. Acad. Sci. U. S. A.* **2015**, *112*, 15054-15059.

(21) Yoshida, M.; Suzuki, R.; Zhang, Y.; Nakano, M.; Iwasa, Y. Memristive Phase Switching in Two-Dimensional 1T-TaS$_2$ Crystals. *Sci. Adv.* **2015**, *1*, e1500606.

(22) Yoshida, M.; Gokuden, T.; Suzuki, R.; Nakano, M.; Iwasa, Y. Current Switching of Electronic Structures in Two-Dimensional 1T−TaS$_2$ Crystals. *Phys. Rev. B* **2017**, *95*, 121405.

(23) Liu, G.; Debnath, B.; Pope, T. R.; Salguero, T. T.; Lake, R. K.; Balandin, A. A. A Charge-Density-Wave Oscillator Based on an Integrated Tantalum Disulfide-Boron Nitride-Graphene Device Operating at Room Temperature. *Nat. Nanotechnol.* **2016**, *11*, 845-850.

(24) Liu, G.; Zhang, E. X.; Liang, C. D.; Bloodgood, M. A.; Salguero, T. T.; Fleetwood, D. M.; Balandin, A. A. Total-Ionizing-Dose Effects on Threshold Switching in 1T-TaS$_2$ Charge Density Wave Devices. *IEEE Electron Device Lett.* **2017**, *38*, 1724-1727.

(25) Khitun, A.; Liu, G.; Balandin, A. A. Two-Dimensional Oscillatory Neural Network Based on Room-Temperature Charge-Density-Wave Devices. *IEEE Trans. Nanotechnol.* **2017**, *16*, 860-867.

16

(26) Zhao, R.; Wang, Y.; Deng, D.; Luo, X.; Lu, W. J.; Sun, Y. P.; Liu, Z. K.; Chen, L. Q.; Robinson, J. Tuning Phase Transitions in 1T-TaS$_2$ *via* the Substrate. *Nano Lett.* **2017**, *17*, 3471-3477.

(27) Vaskivskyi, I.; Mihailovic, I. A.; Brazovskii, S.; Gospodaric, J.; Mertelj, T.; Svetin, D.; Sutar, P.; Mihailovic, D. Fast Electronic Resistance Switching Involving Hidden Charge Density Wave States. *Nat. Commun.* **2016**, *7*, 11442.

(28) Liu, G.; Rumyantsev, S.; Bloodgood, M. A.; Salguero, T. T.; Balandin, A. A. Low-Frequency Current Fluctuations and Sliding of the Charge Density Waves in Two-Dimensional Materials. *Nano Lett.* **2018**, *18*, 3630-3636.

(29) Peierls, R. E. *Quantum Theory of Solids*; Oxford University Press: New York, 1955; pp 108-112.

(30) Bae, M. H.; Ong, Z. Y.; Estrada, D.; Pop, E. Imaging, Simulation, and Electrostatic Control of Power Dissipation in Graphene Devices. *Nano Lett.* **2010**, *10*, 4787-4793.

(31) Grosse, K. L.; Bae, M. H.; Lian, F.; Pop, E.; King, W. P. Nanoscale Joule Heating, Peltier Cooling and Current Crowding at Graphene-Metal Contacts. *Nat. Nanotechnol.* **2011**, *6*, 287-290.

(32) Nuez-Regueiro, M. D.; Lopez-Castillo, J. M.; Ayache, C. Thermal Conductivity of 1T-TaS$_2$ and 2H-TaSe$_2$. *Phys. Rev. Lett.* **1985**, *55*, 1931-1934.

(33) Yamane, T.; Nagai, N.; Katayama, S.; Todoki, M. Measurement of Thermal Conductivity of Silicon Dioxide Thin Films Using a 3ω Method. *J. Appl. Phys.* **2002**, *91*, 9772-9776.

(34) Lee, S. M.; Cahill, D. G. Heat Transport in Thin Dielectric Films. *J. Appl. Phys.* **1997**, *81*, 2590-2595.

(35) Gurrum, S. P.; King, W. P.; Joshi, Y. K.; Ramakrishna, K. Size Effect on the Thermal Conductivity of Thin Metallic Films Investigated by Scanning Joule Expansion Microscopy. *J. Heat Transfer* **2008**, *130*, 082403.

(36) Rajani, K. V.; Daniels, S.; McNally, P. J.; Lucas, F. O.; Alam, M. M. Ultrathin Chromium Transparent Metal Contacts by Pulsed DC Magnetron Sputtering. *Phys. Status Solidi A* **2010**, *207*, 1586-1589.

(37) Goff, J. F. Lorenz Number of Chromium. *Phys. Rev. B* **1970**, *1*, 1351-1362.

(38) Chen, G.; Hui, P. Thermal Conductivities of Evaporated Gold Films on Silicon and Glass. *Appl. Phys. Lett.* **1999**, *74*, 2942-2944.

(39) Schroder, D. K. *Semiconductor Material and Device Characterization*; John Wiley & Sons: Hoboken, 2006; pp 138-141.

(40) Hoppensteadt, F. C.; Izhikevich, E. M. Pattern Recognition *via* Synchronization in Phase-Locked Loop Neural Networks. *IEEE Trans. Neural Netw.* **2000**, *11*, 734-738.

(41) Liu, X.; Wang, D. L. Range Image Segmentation Using a Relaxation Oscillator Network. *IEEE Trans. Neural Netw.* **1999**, *10*, 564-573.

(42) Wijekoon, J. H.; Dudek, P. Compact Silicon Neuron Circuit with Spiking and Bursting Behaviour. *Neural Netw.* **2008**, *21*, 524-534.

(43) Moser, J.; Barreiro, A.; Bachtold, A. Current-Induced Cleaning of Graphene. *Appl. Phys. Lett.* **2007**, *91*, 163513.
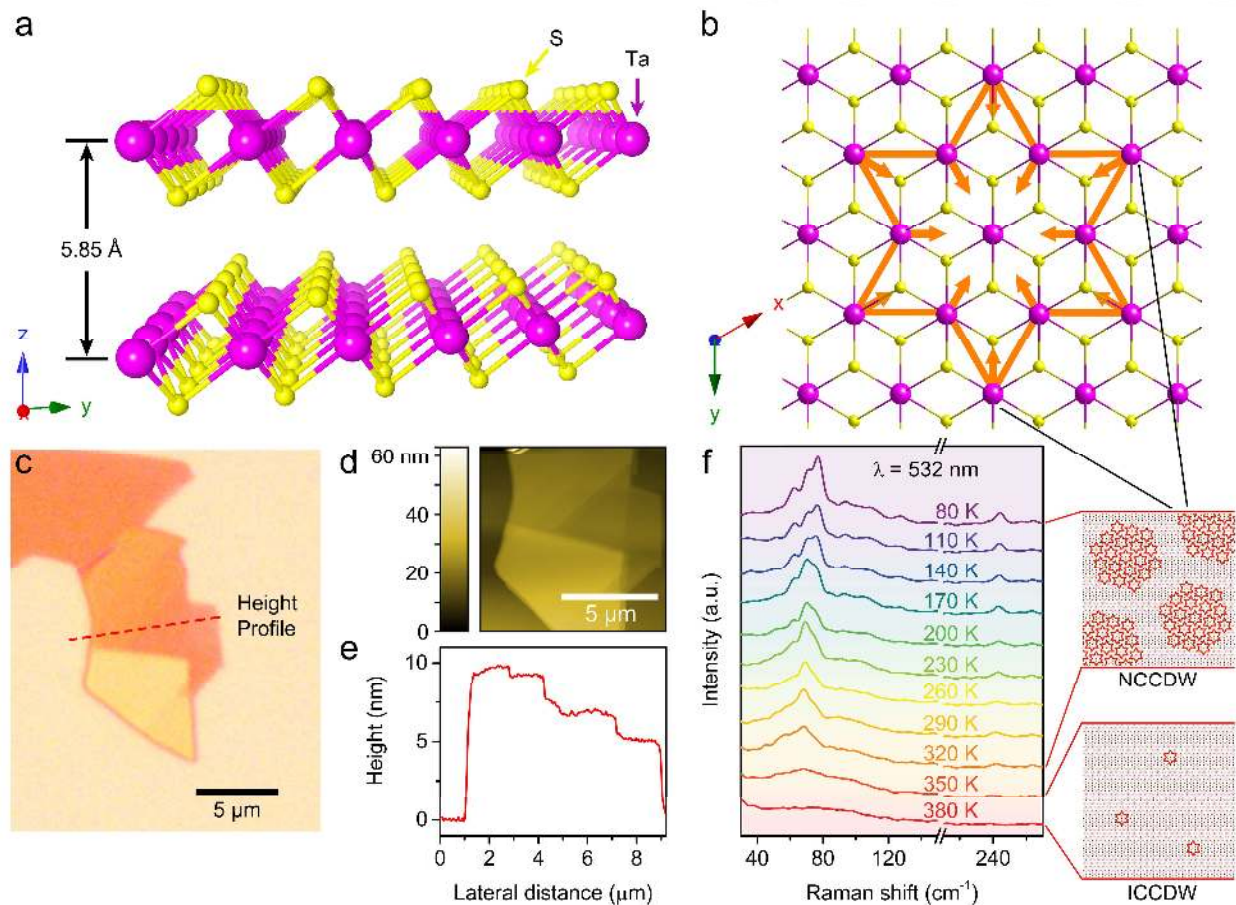
Figure 1. Structure of 1T-TaS$_2$ and basic characterizations. (a) The crystal structure of layered 1T-TaS$_2$, where Ta atoms are in magenta and S atoms are in yellow. (b) A top view of the David star arising from the lattice distortion. (c) A typical optical image of 1T-TaS$_2$ exfoliated onto the SiO$_2$/Si substrate. (d) An AFM image of the sample. (e) The cross-section height profile along the dashed red line in (c). (f) Left: temperature-dependent Raman spectra of a 9.4-nm-thick 1T-TaS$_2$. Right: an illustration of the CDW phase at different temperatures. For NCCDW, there are CDW domains formed by David stars. For ICCDW, the lattice is slightly distorted and no CDW domain exists.
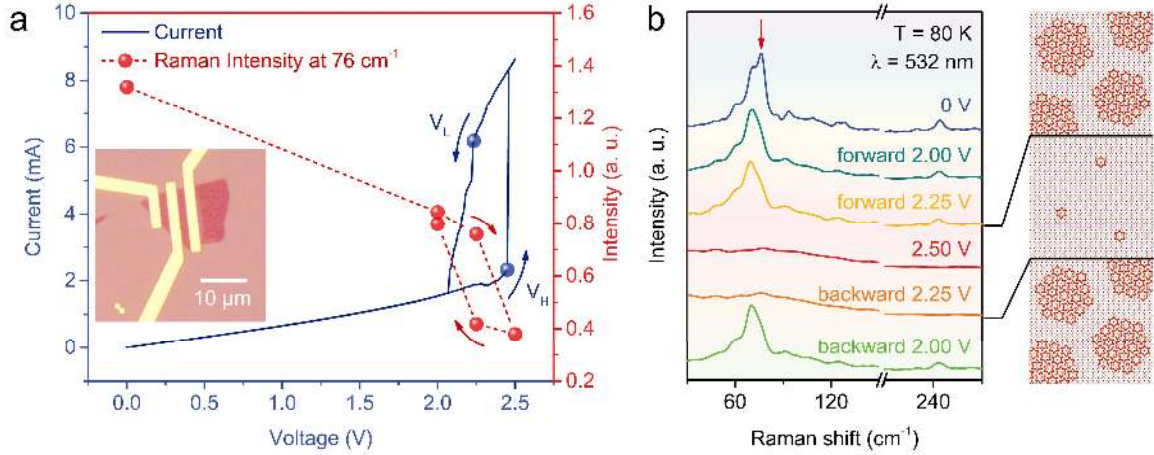
Figure 2. *In situ* Raman spectra. (a) Black solid line: the *I-V* curve of a 9.4-nm-thick 1T-TaS$_2$ device, where the upper and lower threshold voltages (V_H and V_L) are marked with black dots. Red dash line: *in situ* Raman signal intensity at 76 cm^{-1} under the 532-nm excitation at 80 K. Inset: a typical optical image of the 1T-TaS$_2$ device. (b) Left: *in situ* Raman spectra of 1T-TaS$_2$ under the 532-nm excitation at 80 K. The highest A$_{1g}$ peak at 76 cm^{-1} at 0 V is marked by the red arrow. Right: an illustration of CDW phase under different voltages.
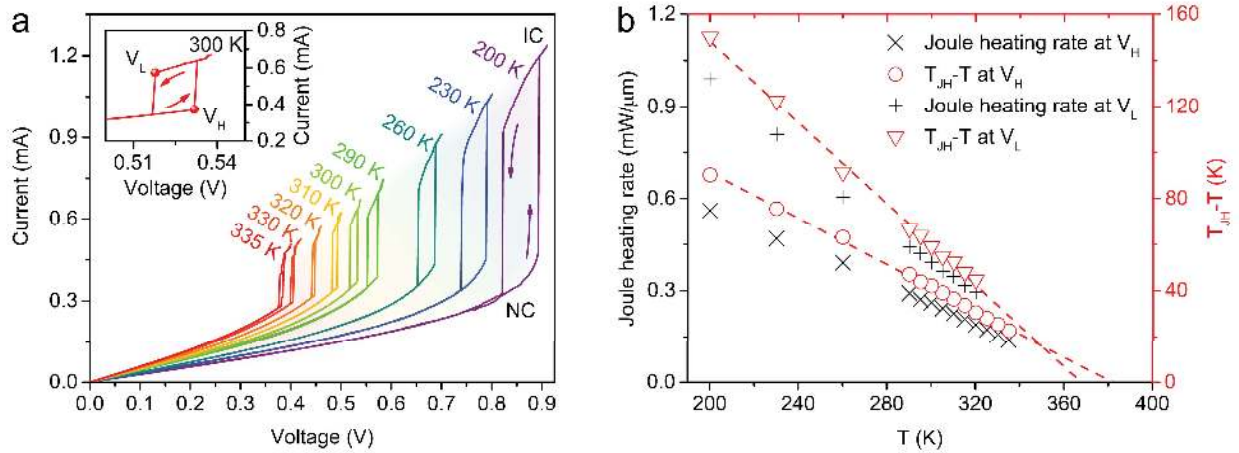
Figure 3. Temperature-dependent *I-V* behavior. (a) Temperature-dependent *I-V* curves of 11.8-nm-thick 1T-TaS$_2$ measured by the two-probe method. Inset: *I-V* curve with V_H and V_L marked by red dots. (b) Joule heating rate and $T_{JH} - T$ at V_H and V_L at different temperatures.
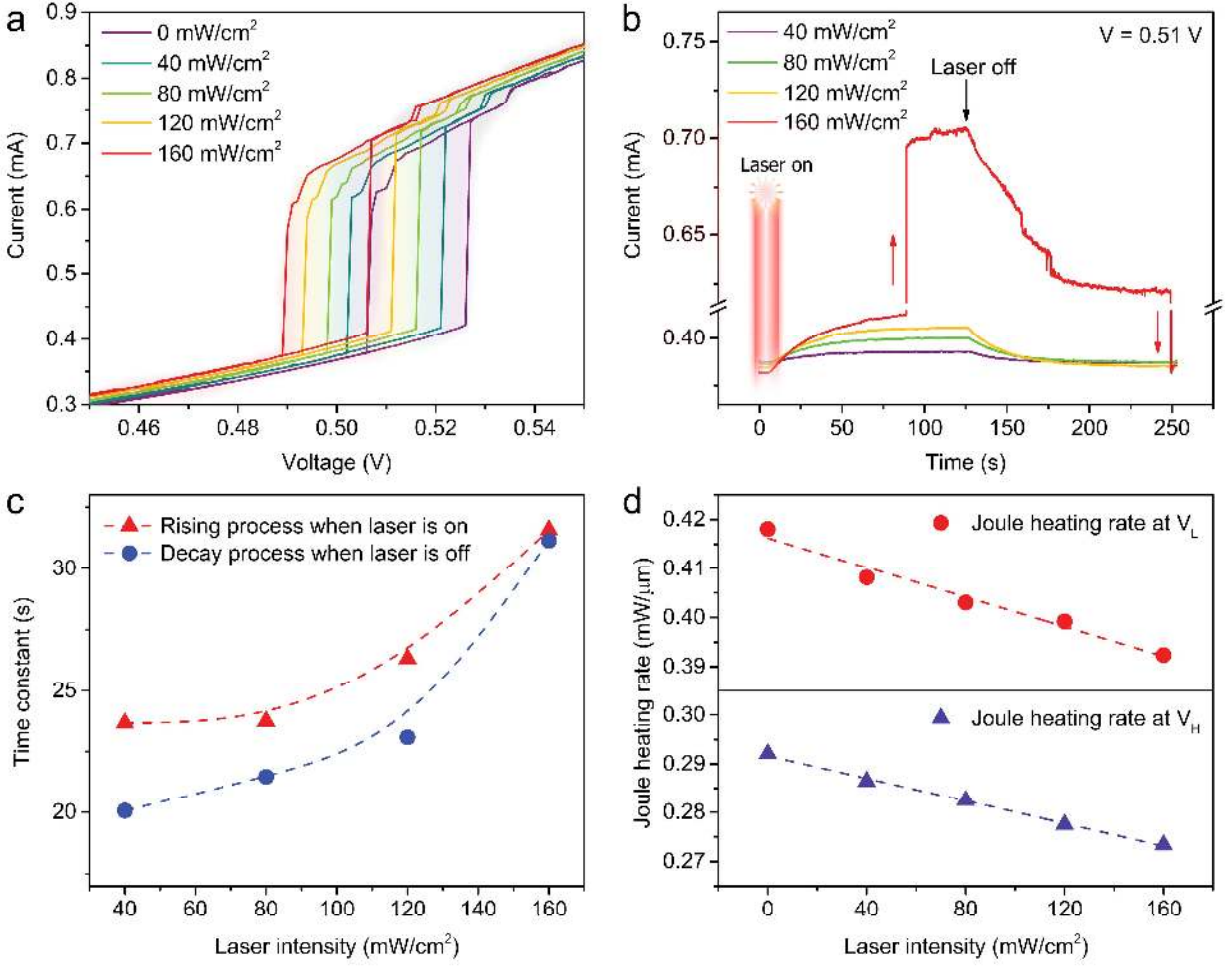
Figure 4. Laser-tuned electric-field-induced CDW phase transition in an 11.8-nm-thick 1T-TaS$_2$ sample at the room temperature. (a) The *I-V* curve shifts under the 635-nm laser. (b) Time evolution of the current with laser on/off at fixed voltage bias (0.51 V) under different laser intensities. (c) Laser-intensity-dependent time constant of the current rising and decaying process. (d) The Joule heating rate at phase transition point V_H and V_L at different laser intensities.
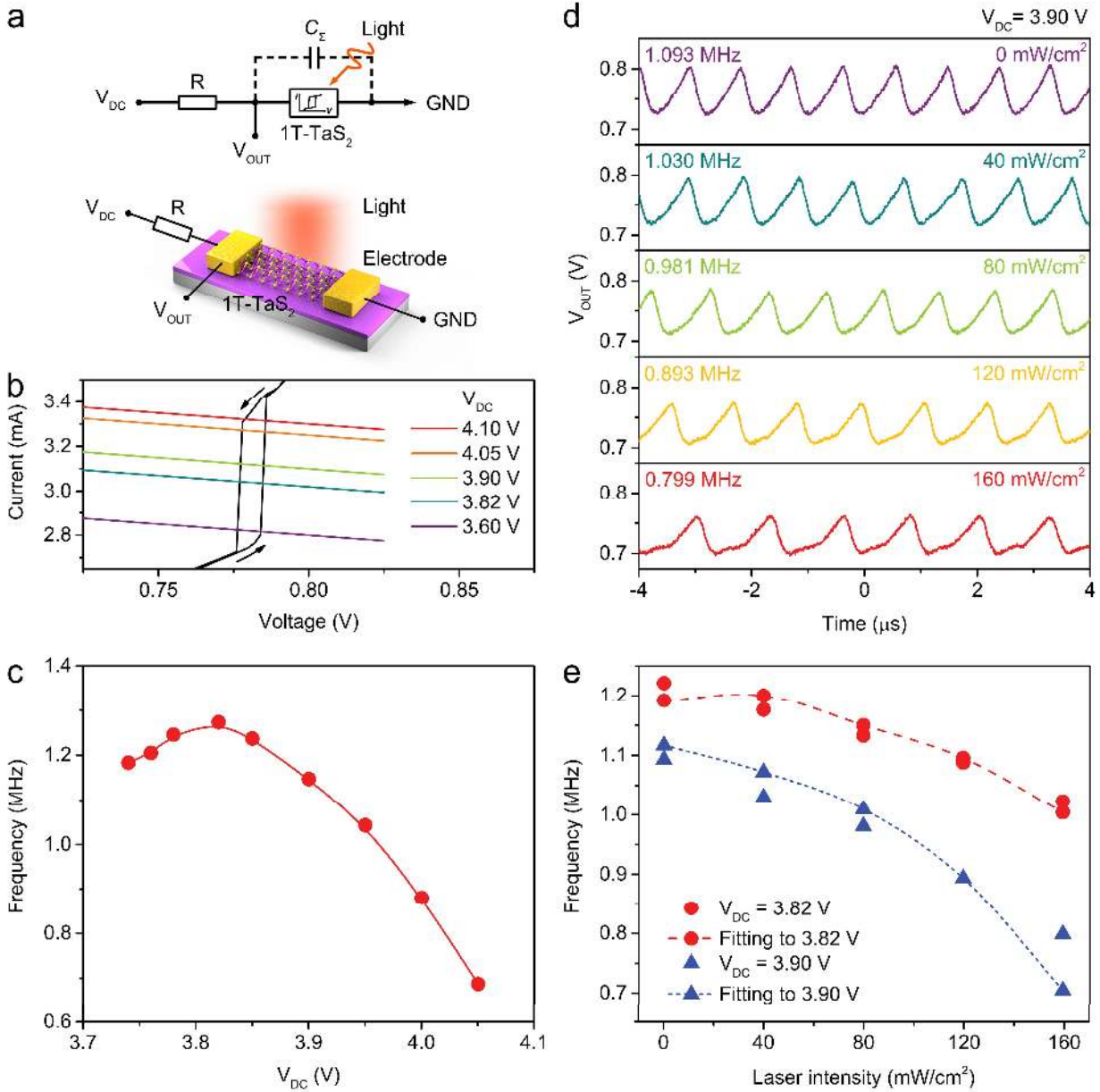
Figure 5. 1T-TaS$_2$ based oscillator tuned by laser. (a) The 1T-TaS$_2$ based oscillator circuit and its three-dimensional view. (b) The *I-V* characteristic of 1T-TaS$_2$ and the load lines of 1T-TaS$_2$ in the oscillator circuit under different input voltages. (c) The oscillation frequency of the output voltage changes with the input voltage. (d) Voltage oscillations under different laser intensities at a fixed input voltage. (e) The oscillation frequency tuned by the laser intensity.

For Table of Contents Only